

Inverse design optimization framework via a two-step deep learning approach: application to a wind turbine airfoil

Sunwoong Yang^a, Sanga Lee^b, Kwanjung Yee^{a*}

^a Seoul National University, Seoul 08826, Republic of Korea

^b Korea Institute of Industrial Technology, Incheon 21999, Republic of Korea

sunwoongy@gmail.com

Abstract

Though inverse approach is computationally efficient in aerodynamic design as the desired target performance distribution is specified, it has some significant limitations that prevent full efficiency from being achieved. First, the iterative procedure should be repeated whenever the specified target distribution changes. Target distribution optimization can be performed to clarify the ambiguity in specifying this distribution, but several additional problems arise in this process such as loss of the representation capacity due to parameterization of the distribution, excessive constraints for a realistic distribution, inaccuracy of quantities of interest due to theoretical/empirical predictions, and the impossibility of explicitly imposing geometric constraints. To deal with these issues, a novel inverse design optimization framework with a two-step deep learning approach is proposed. A variational autoencoder and multi-layer perceptron are used to

generate a realistic target distribution and predict the quantities of interest and shape parameters from the generated distribution, respectively. Then, target distribution optimization is performed as the inverse design optimization. The proposed framework applies active learning and transfer learning techniques to improve accuracy and efficiency. Finally, the framework is validated through aerodynamic shape optimizations of the airfoil of a wind turbine blade, where inverse design is actively being applied. The results of the optimizations show that this framework is sufficiently accurate, efficient, and flexible to be applied to other inverse design engineering applications.

Keywords: inverse design optimization, multi-layer perceptron, variational autoencoder, wind turbine airfoil

1. Introduction

Recent advances in high-performance computing have enabled aerodynamic engineers to use high-fidelity analyses, offering a wide range of options in the aerodynamic design process. Accordingly, numerous novel design methodologies have been developed, most of which are based on two conventional aerodynamic design methods: inverse and direct design approaches [1-3]. In particular, inverse design is computationally efficient in that the desired target performance distribution is already defined and the corresponding design shape can be calculated with a few iterations

coupled with a flow solver [4-6].

However, the inverse method also has a critical disadvantage: whenever the target distribution changes, an iterative process to find the design shape matching the target distribution should be repeated. Considering that most design stages require significant trial and error, this process undermines the efficiency of the inverse design as it increases the requirement of computational resources. Therefore, several researchers have used a surrogate model in inverse design to avoid this iterative process. Recently, artificial neural network (ANN) surrogate models have been widely used owing to their universal approximation property [7]. Kharal and Saleem [8] and Sun et al. [9] used aerodynamic quantities of interest (QoI) as the inputs of an ANN model to obtain airfoil shape parameters as the output in an inverse design procedure. Wang et al. [10] also applied an ANN for the same purpose, but additionally performed dimensional reduction of input data using principal component analysis to reduce the database size required for model training.

These studies have clear advantages as they do not require iterative procedures coupled with the flow solver in the inverse design. However, they still have not provided a solution to another problem: the performance distribution should be specified, which will be used as an input of the inverse design. For an efficient design, an appropriate aerodynamic performance should be defined, which is highly dependent on the designer's engineering knowledge and experience. For instance, the target pressure distribution of the airfoil prescribed by different engineers will vary dramatically

depending on their engineering skills.

This ambiguity in specifying the target distribution has prompted researchers to optimize it. Obayashi and Takanashi [11] and Kim and Rho [12] used control points-based techniques to parameterize the pressure distributions, and then optimized the distribution using a genetic algorithm (GA). In these inverse design optimization processes, the aerodynamic QoI were obtained through theoretical/empirical predictions, and a number of constraints were imposed to ensure the reality of the pressure distribution. For instance, Obayashi and Takanashi [11] estimated the viscous drag using the Squire–Young empirical formula and imposed six constraints for realistic pressure coefficient (C_p) distributions. Though these studies attempted to deal with the fundamental limitations of the inverse design method, the following problems still exist:

- 1) loss of the diverse representation capacity of the C_p distribution due to parameterization; 2) excessive constraints to ensure a realistic C_p distribution; 3) discrepancies between the QoI predicted theoretically/empirically and those calculated using a flow solver; and 4) impossibility of explicitly imposing geometric constraints on the design shape. To address the limitations of the representation capacity, QoI discrepancies, and excessive constraints, Zhu et al. [13] proposed an inverse design optimization method using proper orthogonal decomposition (POD). They reduced the dimension of the C_p distribution data via POD and used the support vector regression (SVR) model to predict the aerodynamic performance of the airfoil from the reduced C_p data. Then, a GA was implemented to optimize the C_p distribution coupled with POD and SVR. Finally, the optimized pressure was passed on to the conventional inverse design process, and the corresponding airfoil shape was obtained in an iterative manner

coupled with the flow solver. However, the limitation of geometric constraints has not been addressed because the prediction of the design shape is separated from the pressure optimization process. Therefore, when the shape predicted in the inverse design process violates geometric constraints, the design process should be traced back to the optimization process. Additionally, at the optimum solution, the discrepancy between the pressure distributions from prediction and calculation is noticeable, which indicates the low accuracy of its framework. This is because there is no way to take into account the reality of the distribution, such that the optimized pressure distribution may not have a solution. Finally, as the inputs of the SVR are the reduced POD mode coefficients, the accuracy of the regression inevitably decreases.

The drawbacks of the previous inverse design studies presented so far should be overcome by applying novel techniques in that computational efficiency, an essential advantage of inverse design, cannot be fully exploited. Therefore, this study proposes an inverse design optimization framework with a two-step deep learning approach. This approach refers to the sequential coupling of two deep learning models: variational autoencoder (VAE) and multi-layer perceptron (MLP). The limitations of previous inverse design studies can be eliminated using the proposed framework as follows:

- 1) The conventional inverse design process is substituted with the MLP surrogate model so that the iterations coupled with the flow solver are not required.
- 2) From the target distribution, the MLP surrogate model not only predicts the design shape, but also the QoI. Therefore, a theoretical/empirical assumption is not required for predicting the QoI, and the geometric constraints can be handled directly as QoI in the

target distribution optimization process.

3) For the inverse design optimization, a realistic target performance distribution is generated using a VAE deep generative model so that the loss of the diverse representation capacity due to parameterization of the distribution is mitigated and excessive constraints for the realistic distribution are not required.

In the two-step deep learning approach, the VAE and MLP were used to generate a realistic target distribution and to predict the QoI and shape parameters from the generated distribution, respectively. Then, target distribution optimization was performed as the inverse design optimization based on this approach. Active learning and transfer learning strategies were applied to improve the accuracy of the two-step approach-based optimization at a reasonable computational cost. The proposed inverse design optimization framework via a two-step deep learning approach was validated through aerodynamic shape optimization of the airfoil of a wind turbine blade, where inverse design is actively being applied. Two constrained optimization problems, namely single-objective and multi-objective optimizations, were used to validate the accuracy, robustness, and flexibility of the framework. The results of these practical engineering applications demonstrate that the proposed framework has outstanding accuracy and modeling capability as it successively learned various QoI behaviors. Furthermore, considering that the corresponding framework can be coupled with any numerical solver with arbitrary QoI and design shape, this versatile inverse design framework can be easily extended and applied to any engineering field.

This paper is organized as follows. *Section 2* describes the mathematical background

of two deep learning models used in the inverse design optimization framework. *Section 3* presents the scheme of the proposed framework. In *section 4*, validation of the framework with application to a wind turbine airfoil is performed and the results are discussed. Finally, *section 5* concludes the study, emphasizing the flexibility of the presented framework.

2. Methodology

2.1 Multi-layer perceptron (MLP)

ANNs have been widely used in recent engineering design studies in that they can successfully learn complex nonlinear correlations between inputs and outputs [14, 15]. Furthermore, they are known for their efficiency in training high-dimensional problems with massive amounts of data. Among several ANN models, the MLP is the most common structure as it can learn various nonlinear physical phenomena using hidden layers; according to the universal approximation theorem, a neural network with a single hidden layer and finite nodes can approximate any continuous function [7]. In the inverse design optimization framework investigated in this study, an MLP model with these advantages was used as a regression surrogate model. This section presents a brief background of this model.

The MLP model passes on information received from the input layer to the output layer through the feed-forward process. Information transfer between each layer is performed through an affine transformation using weights and biases, as given in Eq. (1) (where \mathbf{x} is a vector of nodes at the current layer, \mathbf{W} and \mathbf{b} are the weight matrix and bias vector between the current layer and the next layer, respectively and \mathbf{y} is a vector

of the nodes at the next layer). As it is based on a linear relationship, nonlinearity cannot be modeled irrespective of how many hidden layers are used.

$$\mathbf{y} = \mathbf{W}\mathbf{x} + \mathbf{b}. \quad (1)$$

Modeling of nonlinearity is enabled by imposing activation functions on each layer. Typical examples of the functions include sigmoid, tanh, ReLU, and Leaky ReLU. The ReLU function has been used in numerous studies because it has less saturation problems than sigmoid and tanh, and it does not perform expensive exponential operations. However, the ReLU function also has the disadvantage of being non-zero centered; therefore, the Leaky ReLU function is implemented as follows [16]:

$$f(x) = \begin{cases} x & \text{if } x > 0 \\ ax & \text{otherwise} \end{cases}. \quad (2)$$

The MLP model takes an activation function on \mathbf{y} in Eq. (1) and uses it as an input for the next layer to learn nonlinear behavior. This process is repeated until the data of the input layer reach the output layer. However, the final output will be quite different from the value of the training data as there is no training procedure for weights and biases in feed-forward. Accordingly, the weights and biases are trained based on the gradient of the loss function (the error between these two values) using backpropagation. They are updated through this process to reduce the loss function of the model. Feed-forward (which transfers information from input to output) and backpropagation (which updates the model parameters) are repeated iteratively using gradient descent optimization techniques. Several optimization methods can be used, such as Adagrad, RMSprop, and Adam. Adam has been widely used as it combines the strengths of Adagrad and RMSprop;

its advantages are the ability to deal with sparse gradients and non-stationary objectives [17]. When the optimization process reduces the loss function to the desired level, a trained MLP model with fixed weights and biases serves as a surrogate model. Many papers adopting the MLP model have been published in various engineering fields; therefore, only the fundamental contents are presented in this paper. For more details on MLP, refer to Ref. [18].

2.2 *Variational autoencoder (VAE)*

A generative model learns how it is generated from real-world data [19]. In particular, a deep generative model uses neural networks with hidden layers to learn the underlying features of arbitrary data. Generative adversarial network (GAN) [20] and VAE [21] are typical examples of widely used deep generative models. Both models can be regarded as a dimensional reduction technique that learns a compact low-dimensional latent space from high-dimensional original data. Thus, the trained model can be used as a data generator in that it generates high-dimensional output data when it receives a low-dimensional latent variable. However, a GAN has the disadvantage that it is difficult to generate continuous physical data such as pressure distribution and airfoil shape; therefore, auxiliary filters or layers should be used. For instance, Chen et al. [22, 23] added a Bezier layer or a free-form-deformation layer at the end of the generator to enforce the continuity of the generated airfoil using a GAN. In addition, Achour et al. [24] used the Savitzky–Golay filter on the generated airfoil for the same reason. However, when user-defined layers or filters are added to the neural network structure, additional hyperparameters are generated, thereby increasing the engineer’s effort to train the model. Furthermore, a GAN is known to be quite difficult to train owing to

non-convergence, mode collapse, and vanishing gradients [25]. Therefore, in this study, a VAE was used as the data generator for the inverse design optimization. It is easy to train and does not require an extra post-processing technique to ensure continuity of the generated data. It will be shown later that the VAE used for this purpose was trained to generate smooth target distribution data for the inverse design.

The mathematical details of the VAE model are presented below. Note that this section is mainly based on Ref. [21].

Consider a dataset $X = \{x_i\}_{i=1}^N$, which consists of independent and identically distributed N samples of variable x , and the unknown random variable z is for generating x . When generating x from z , variational inference (VI) is applied as the posterior $p_\theta(z|x)$ is intractable due to the intractability of the likelihood $p_\theta(z)$, where θ is a generative model parameter. Here, the approximation function $q_\phi(z|x)$ is used for the sampling instead of the intractable posterior $p_\theta(z|x)$, where ϕ is a variational parameter. Using this approximation, the marginal likelihood $p_\theta(x)$ can be expressed as

$$\begin{aligned}
\log(p_\theta(x)) &= \int \log(p_\theta(x)) q_\phi(z|x) dz \left(\because \int q_\phi(z|x) dz = 1 \right) \\
&= \int \log\left(\frac{p_\theta(x, z)}{p_\theta(z|x)}\right) q_\phi(z|x) dz \left(\because p_\theta(x) = \frac{p_\theta(x, z)}{p_\theta(z|x)} \right) \\
&= \int \log\left(\frac{p_\theta(x, z)}{q_\phi(z|x)} \cdot \frac{q_\phi(z|x)}{p_\theta(z|x)}\right) q_\phi(z|x) dz \\
&= \int \log\left(\frac{p_\theta(x, z)}{q_\phi(z|x)}\right) q_\phi(z|x) dz + \int \log\left(\frac{q_\phi(z|x)}{p_\theta(z|x)}\right) q_\phi(z|x) dz.
\end{aligned} \tag{3}$$

The second term in the last equation is the Kullback–Leibler (KL) divergence of $q_\phi(z|x)$ from $p_\theta(z|x)$, $KL(q_\phi(z|x) || p_\theta(z|x))$, and it is impossible to calculate this term. Furthermore, because this term is always non-negative by its definition, the first term in the last equation becomes the lower bound on the marginal likelihood. Therefore, the maximization of the marginal likelihood can be replaced by the problem of maximizing the lower bound according to the evidence lower bound (ELBO). The corresponding lower bound term can be divided as follows:

$$\begin{aligned}
& \int \log \left(\frac{p_\theta(x, z)}{q_\phi(z|x)} \right) q_\phi(z|x) dz \\
&= \int \log \left(\frac{p_\theta(x|z)p_\theta(z)}{q_\phi(z|x)} \right) q_\phi(z|x) dz \quad (\because p_\theta(x, z) = p_\theta(x|z)p_\theta(z)) \\
&= \int \log(p_\theta(x|z)) q_\phi(z|x) dz - \log \left(\frac{q_\phi(z|x)}{p_\theta(z)} \right) q_\phi(z|x) dz \\
&= \mathbb{E}_{q_\phi(z|x)} [\log(p_\theta(x|z))] - \log \left(\frac{q_\phi(z|x)}{p_\theta(z)} \right) q_\phi(z|x) dz.
\end{aligned} \tag{4}$$

Therefore, maximization of the marginal likelihood $p_\theta(x)$ means maximizing the last equation of Eq. (4), where the first term is the reconstruction error of x through the posterior distribution (approximation function) $q_\phi(z|x)$ and the likelihood $p_\theta(x|z)$. The second term is the KL divergence of $q_\phi(z|x)$ from the prior $p_\theta(z)$, $KL(q_\phi(z|x) || p_\theta(z))$. In summary, the VAE model can be trained using the loss function consisting of the reconstruction error of data x and the KL divergence of the approximation function from the prior.

In the derived loss function above, the approximation function $q_\phi(z|x)$ represents the dimensionality reduction procedure using an encoder (from original data to latent variable) and the likelihood $p_\theta(x|z)$ represents the dimensionality reconstruction procedure using a decoder (from latent variable to original data). To represent the intractability of these procedures, neural networks with hidden layers (MLP) are used to realize the encoder and decoder of the VAE. This explains why a VAE has a similar structure to a standard autoencoder (AE) [26]. However, the main difference is the latent

space variable z . In an AE, the output of the encoder is used as a latent variable deterministically. On the other hand, the encoder of the VAE outputs a set of distribution parameters consisting of the mean (μ_i) and standard deviation (σ_i) of the Gaussian distribution, and the latent space is sampled with randomness; to sample a J -dimensional latent variable z , the same number of sets $\{\mu_i, \sigma_i\}$ is required. However, because the gradients cannot be calculated in this random sampling process, model training through backpropagation becomes impossible; therefore, a reparameterization trick is applied (refer to Ref. [27] for more information about this trick). The latent variable z , which is assumed to take the form of the Gaussian distribution, can be expressed as follows:

$$z_i = \mu_i + \sigma_i^2 \odot \epsilon \text{ and } \epsilon \sim N(0,1). \quad (5)$$

As presented earlier, the loss function for training the VAE model consists of a reconstruction error and the KL divergence of the approximation function from the prior. The reconstruction error can be calculated using the binary cross entropy between the original data and reconstructed data from the VAE (reconstructed data refers to data after the original data goes through the encoder and decoder of the VAE). Then, to calculate the $KL(q_\phi(z|x)||p_\theta(z))$ term, $q_\phi(z|x_i) \sim N(\mu_i, \sigma_i^2)$ and $p_\theta(z) \sim N(0,1)$ are assumed. Finally, the KL divergence in the loss function for the datapoint x_i can be expressed as follows, where J is the dimensionality of the latent variable z :

$$\mathcal{L}(\theta, \phi; x_i) = \frac{1}{2} \sum_{j=1}^J (1 + \log((\sigma_i^j)^2) - (\mu_i^j)^2 - (\sigma_i^j)^2). \quad (6)$$

Backpropagation with respect to the loss function (composed of reconstruction error and

KL divergence) enables the decoder of the VAE to be trained to generate realistic data.

The flowchart of the VAE is shown in Fig. 1.

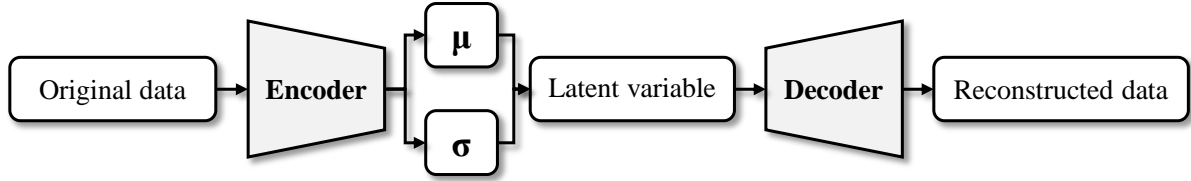


Fig. 1 Flowchart of the variational autoencoder (VAE)

3. Inverse design optimization framework

3.1 Two-step deep learning approach

This section demonstrates the two-step deep learning approach, which connects the VAE and MLP models. First, the VAE was trained with the target performance distributions of the training data. When training has been completed, only the decoder part of the VAE model was used; it operates as a data generator that receives a low-dimensional latent variable and outputs a realistic high-dimensional target distribution. Then, the MLP was trained to predict the QoI and shape parameters from the target distribution. This regression process is more efficient and accurate compared with previous inverse design studies in that there is no iteration and theoretical/empirical assumptions (prediction was performed almost in real-time). In this study, these two deep learning models, the decoder of the VAE and MLP, were utilized sequentially; the decoder generates the distribution once it receives the latent variable, and the MLP outputs the QoI and shape parameters from this generated distribution.

This structure refers to a two-step deep learning approach and its flowchart is shown in Fig. 2.

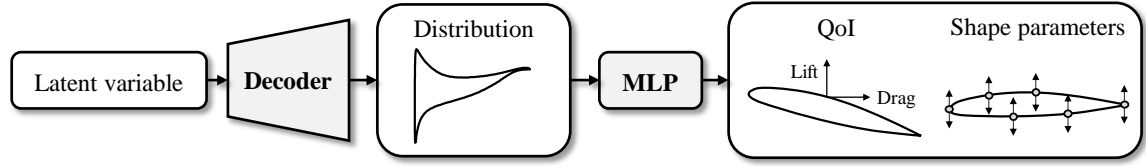


Fig. 2 Flowchart of the two-step deep learning approach

3.2 Target distribution optimization

The two-step deep learning approach allows mapping from the latent space of the target performance distribution to the QoI and shape parameters. Therefore, the optimization of the target distribution can be performed based on this approach. The inputs of the corresponding approach (latent variables) were used as the optimization variable, and the outputs (QoI and shape parameters) as the objective functions and constraints. In this study, because the shape parameters were incorporated into the target distribution optimization procedure, geometric constraints can be imposed directly as shape parameters. At the end of the optimization, numerical validation was performed by comparing the QoI predicted using the two-step approach and calculated using the numerical solver at the optimum solutions. The inverse design optimization framework is terminated when the differences in these values satisfy the error criterion. If not, the process described in *section 3.3* is repeated until it is satisfied.

3.3 Active learning and transfer learning

Model training and optimization were performed according to the framework presented so far based on the initial training data, making it unlikely to meet the desired accuracy at

once. Therefore, studies that perform surrogate-based optimization usually add training data repeatedly to increase the accuracy of the surrogate model. This technique is called the active learning strategy and was adopted in this study for an accurate inverse design optimization framework [28, 29]. When the error criterion at optimum solutions is not satisfied (as presented at the end of *section 3.2*), these solutions were added to the previous dataset and the deep learning models were trained again. In this procedure, the designs added at every iteration are always incorporated in the training data because adding the optimum designs of the previous iteration to the test dataset makes the active learning strategy becomes meaningless as information on these added designs cannot be reflected in the update process. Then, optimization and numerical validation were performed based on these retrained models. This active learning strategy continues until the error between the QoI from the two-step deep learning approach and those from the numerical solver are reduced such that they satisfy a predefined error criterion.

Although the active learning process was applied to efficiently improve the accuracy of the framework, restarting model training with randomly initialized weights and biases at every iteration can severely degrade the computational efficiency. Moreover, in general, when adding new data via active learning, the training model is not significantly updated compared with the previous iteration, as a small amount of data is added compared with existing data. Therefore, this study used a parameter-based transfer learning strategy. This technique ensures that the weights and biases of the previously trained models are transferred to the models to be newly trained [30, 31]. These two strategies improve the accuracy of the presented framework at reasonable computational resources; the computational cost of repetitive model training for accuracy (active

learning) is reduced through transfer learning. The flowchart of the inverse design optimization framework, which summarizes the contents of *sections 3.1–3.3*, is shown in Fig. 3.

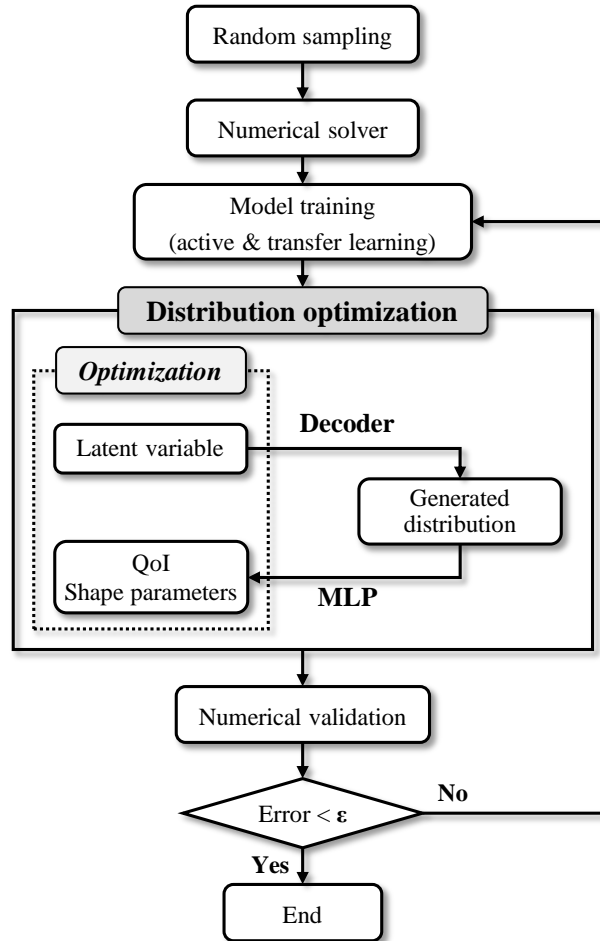


Fig. 3 Flowchart of the inverse design optimization framework

4. Framework validation: optimization of the airfoil for wind turbine blade

The proposed inverse design optimization framework can be applied to all inverse design problems in any engineering field. Inverse design is actively being applied to wind turbine design [32-34]; therefore, to verify the accuracy, effectiveness, and

robustness of this framework, airfoil optimization of a megawatt-class wind turbine was chosen as the application. Structural and aerodynamic performances are mainly considered in the airfoil design of a wind turbine blade. In particular, the airfoil at the tip blade is known to be critical to the aerodynamic performance of the blade. This study aims to optimize the airfoil of the blade's outer part, mostly taking into account its aerodynamic properties (structural performance is indirectly considered via the airfoil area). Single-objective and multi-objective optimizations were performed to demonstrate the versatility of the proposed framework in various optimization problems. The following sections describe the optimization problem (*section 4.1*), architectures of the two-step deep learning models used in the inverse design optimization (*section 4.2*), and the results and discussion of the single-objective and multi-objective optimizations (*sections 4.3 and 4.4*).

4.1 Optimization of the airfoil of a wind turbine blade

This section presents the optimization problem of the airfoil of a wind turbine blade tip region. *Section 4.1.1* presents the validation of the numerical flow solver used in this study, and *section 4.1.2* presents the problem definition for the optimization.

4.1.1 Flow solver

Xfoil is a two-dimensional panel code capable of viscous/inviscid analysis, and it derives very accurate results in a very short time when used appropriately [35]. Because a wind turbine operates at relatively low Reynolds numbers, numerous wind turbine airfoil design studies have used this solver [36-38]. In this study, Xfoil was adopted to calculate the aerodynamic QoI with reasonable computational cost. It should be noted that the proposed

inverse design optimization framework can be coupled with any numerical solver with arbitrary QoI.

Although Xfoil is a well-known and widely used solver, we performed solver validation using experimental results [39]. The experimental data are based on the GA(W)-1 airfoil with Reynolds of 6.3×10^6 , Mach of 0.15, and angle of attack of 8.02° (the flow conditions of the validation are intended to be similar to those of subsequent airfoil optimizations). It was confirmed that this flow solver is appropriate for the wind turbine airfoil optimization performed in this study as it predicts a pressure distribution almost identical to that from experiments (Fig. 4).

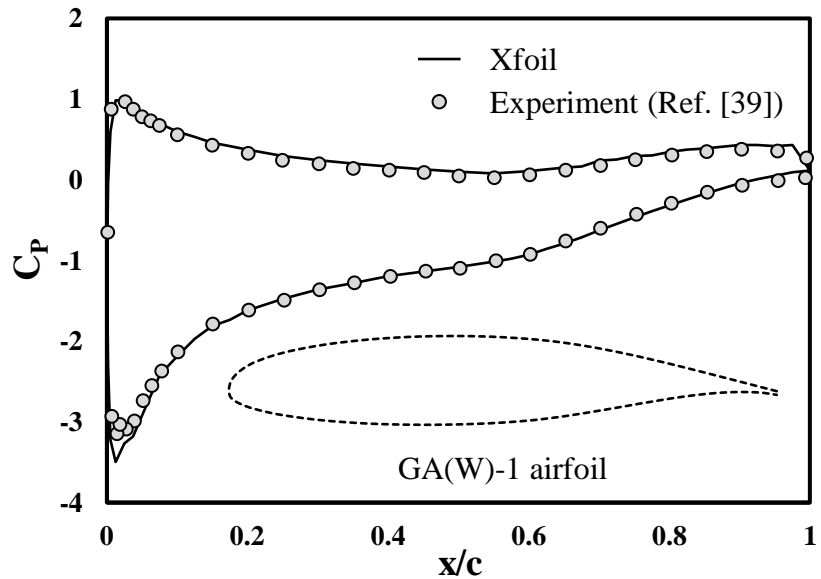


Fig. 4 Comparison of pressure distribution from Xfoil and experimental results in Ref. [39] (used airfoil is also visualized)

4.1.2 Optimization problem definition

Before performing the optimization, the optimization problem should be defined first. There are numerous parameterization methods for representing the airfoil shape, such as PARSEC, B-spline, and class-shape transformation (CST) [40-42]. In this study, PARSEC parameters were adopted as they were originally introduced owing to their close relationship with the aerodynamic characteristics [43]. There are 11 PARSEC variables; six of them were used as shown in Fig. 5, namely $R_{L.E.}$ (leading-edge radius), X_{up} (x-coordinate of the upper crest), Z_{up} (z-coordinate of the upper crest), X_{low} (x-coordinate of the lower crest), Z_{low} (z-coordinate of the lower crest), and $Z_{T.E.}$ (z-coordinate of the trailing-edge). These variables were selected from the prior sensitivity test, which demonstrated that they have a significant impact on the flow characteristics, whereas the other five PARSEC variables have little impact. The corresponding multi-dimensional design space to be explored in the optimization process is summarized in Table 1 (the baseline airfoil shape is selected as the median value of each variable's range).

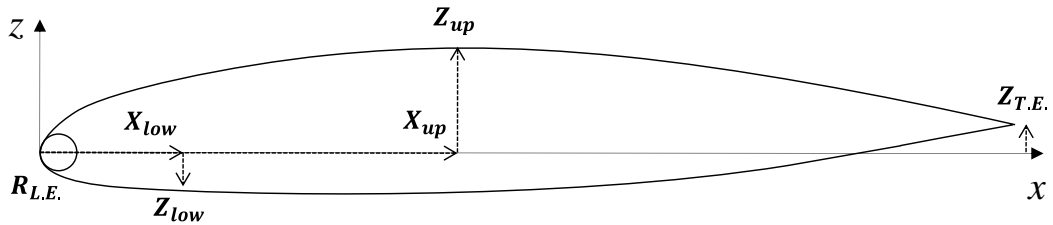


Fig. 5 Shape parameters for representing the airfoil: six PARSEC parameters

Table 1 Design space of the six airfoil shape parameters: the baseline airfoil is selected as the median value of each range

Design variables	Lower bound	Baseline	Upper bound
$R_{L.E.}$	0.015	0.0275	0.04
X_{up}	0.3	0.375	0.45
Z_{up}	0.09	0.12	0.15
X_{low}	0.3	0.375	0.45
Z_{low}	-0.15	-0.12	-0.09
$Z_{T.E.}$	-0.02	0	0.02

When the airfoil shape is determined using PARSEC parameters, flow analysis proceeds. Xfoil is executed under predefined settings (including the flight conditions), and the aerodynamic QoI that will be used as objective functions or constraints in the optimization are extracted. The corresponding flight conditions, objective functions, and constraints for single-objective and multi-objective airfoil optimizations are summarized in Table 2. In the single-objective optimization, the objective is to maximize the lift to drag ratio (L/D), which is the most crucial factor for the aerodynamic efficiency. Furthermore, some constraints are considered to exclude undesirable performance [44]: the drag should be less than the baseline value, the pitching moment coefficient at $c/4$ should be greater than the specific value to limit blade torsion, and the area should be at least 90% of the baseline area to prevent serious degradation of the structural performance. Note that the geometric constraint (airfoil area in this case) can be directly imposed in this framework as QoI in the target distribution optimization process (PARSEC parameters can also be set as geometric constraints, such as $Z_{up} < 0.15$, but these were realized in this study by limiting the design space). In the multi-objective optimization, the two objectives are to maximize the L/D ratio and airfoil area, considering that the area represents the structural performance. Other constraints are the same as those in the single-objective

optimization.

Table 2 Flight conditions, objective functions, and constraints for single-objective and multi-objective optimizations

Flight conditions	Reynolds number	$6*10^6$
	Mach number	0.25
	Angle of attack	7°
Single-objective optimization	Objective function	Maximize L/D
	Constraints	$C_d < \text{Baseline } C_d$ $C_m > -0.08$ $\text{Area} > 0.9 * \text{Baseline Area}$
Multi-objective optimization	Objective functions	Maximize L/D Maximize Area
	Constraints	$C_d < \text{Baseline } C_d$ $C_m > -0.08$

Then, random sampling was performed to train the MLP and VAE models; the sampled initial design samples were used as the initial training data. Latin hypercube sampling was selected owing to its uniformity in the design space [45]. A total of 500 initial designs were sampled and two deep learning models were trained based on them. Finally, the optimization proceeds using the latent variables of the VAE as the optimization variables, and the QoI and shape parameters as the objective functions and constraints, as shown in Fig. 3. In this study, GA was adopted owing to its efficient global exploration in discontinuous and multimodal problems [46]. For multi-objective optimization, the non-dominated sorting genetic algorithm-II (NSGA-II) was adopted to obtain the diversified Pareto solutions of both objective functions [47]. Both optimization algorithms were implemented using Python package pymoo [48]. When the first optimization ends with two-step deep learning models

trained using 500 initial designs, active learning and transfer learning strategies were repeated iteratively. Because there is only one optimal solution in the single-objective optimization, the single optimal solution is selected as the design to be infilled. On the other hand, there are several optimal solutions for the multi-objective optimization (Pareto solutions). In this case, the leftmost, middle, rightmost designs in the Pareto solutions are selected to be infilled, which is considered adequate to increase the overall accuracy of the Pareto solutions. These criteria for infilling can be determined arbitrarily by the engineer. Through these iterative procedures, the framework consisting of the two deep learning models satisfies the given error criterion. Again, note that the proposed framework can be applied to any inverse design problem (the design shape, corresponding shape parameters, QoI, numerical solver, and optimizer can be selected arbitrarily).

4.2 Architectures of the two-step deep learning models

In the two-step approach, the MLP model was trained to take the C_p distribution as input and output QoI and shape parameters. For the input, all airfoils were discretized to have 199 identical x-coordinates using a hyperbolic tangent function, and the pressure coefficients of the corresponding points were used as the input of the MLP. For the output, six shape parameters ($R_{L.E.}$, X_{up} , Z_{up} , X_{low} , Z_{low} , and $Z_{T.E.}$) and four QoI (L/D , C_d , C_m , and area) were concatenated to form the 10 output nodes. Finally, the MLP has 199 input nodes, 10 output nodes (all the outputs are normalized), and two hidden layers with 100 nodes: the MLP with the corresponding hidden layers was found to have sufficient accuracy for the regression in this problem. Then, LeakyReLU activation functions were applied to all the layers for

nonlinearity. Adam was used as the optimizer with the mean square error loss function to train this MLP architecture, and the initial learning rate starts with 0.001. For the first iteration in active learning, 500 initial samples were split into training and test data in the ratio of 8:2 (the same ratio was also used to train the VAE). A total of 30000 epochs with a mini-batch size of 100 were performed using a scheduler that multiplies the learning rate by 0.8 for every 3000 epochs. Because there are no weight or bias values to be used as a reference in the first iteration, they were initialized using He initialization. Then, active and transfer learning were performed. Interestingly, during the MLP training, it was observed that if the parameters of all layers from the previous model were passed, the learning terminates without any meaningful change from the previous model. This is because the number of newly added designs is small compared with that of existing training data, and their effect on the loss function is negligible. Therefore, active learning, which increases the accuracy by appending previous optimum solutions to the current training data, becomes meaningless as their properties are not accurately reflected in the current model. In this study, the parameters of the last layer of the MLP were initialized using He initialization, whereas those of other layers were transferred from the previous model. For subsequent iterations, the required total epochs decreased to 10000 with the same initial learning rate and scheduler as the first iteration, owing to these transfer learning techniques. As a result, training the MLP in the first iteration using a personal computer (Intel Core i7-8700 3.2 GHz with 16 GB 2400 MHz DDR4 RAM) took 508 s, and subsequent iterations took an average of 186 s using Python package PyTorch [49].

For the VAE model, the 199 C_p data previously inputted into the MLP were used as inputs and outputs (VAE has the same input and output). The 199-dimensional input data

was reduced to four-dimensions using an encoder with hidden layers of 120, 60, and 30 nodes. Herein, the four-dimensions represent distribution parameters for random sampling in the latent space: two for the mean and the other two for the standard deviation of the Gaussian distribution. From these parameters, random sampling was performed and the dimension was reduced to a two-dimensional latent space (to sample a J -dimensional latent variable z , the same number of $\{\mu, \sigma\}$ sets is required as described in *section 3.2*, and J equals 2 in this study). These two-dimensions were again reconstructed to 199-dimensions using a decoder with hidden layers of 30, 60, and 120 nodes. The corresponding architecture of the VAE is shown visually in Fig. 6. As in the MLP, the LeakyReLU activation function and Adam optimizer with mean square error loss function were used. The initial learning rate starts with 0.001, and a total of 30000 epochs were performed with a mini-batch size of 100 and a scheduler multiplying the learning rate by 0.5 for every 5000 epochs. In contrast to the MLP, the situation in which the learning process terminates without reflecting information of newly added designs is hardly observed in the VAE. Therefore, the parameters of all the layers from the previous iteration were transferred to the next iteration. For subsequent iterations, a total of 10000 epochs were performed with the same initial learning rate and scheduler as the first iteration. As a result, training the VAE in the first iteration took 627 s, and subsequent iterations took an average of 226 s. All the hyperparameters of the MLP and VAE mentioned in this section were applied identically in the single-objective and multi-objective optimization.

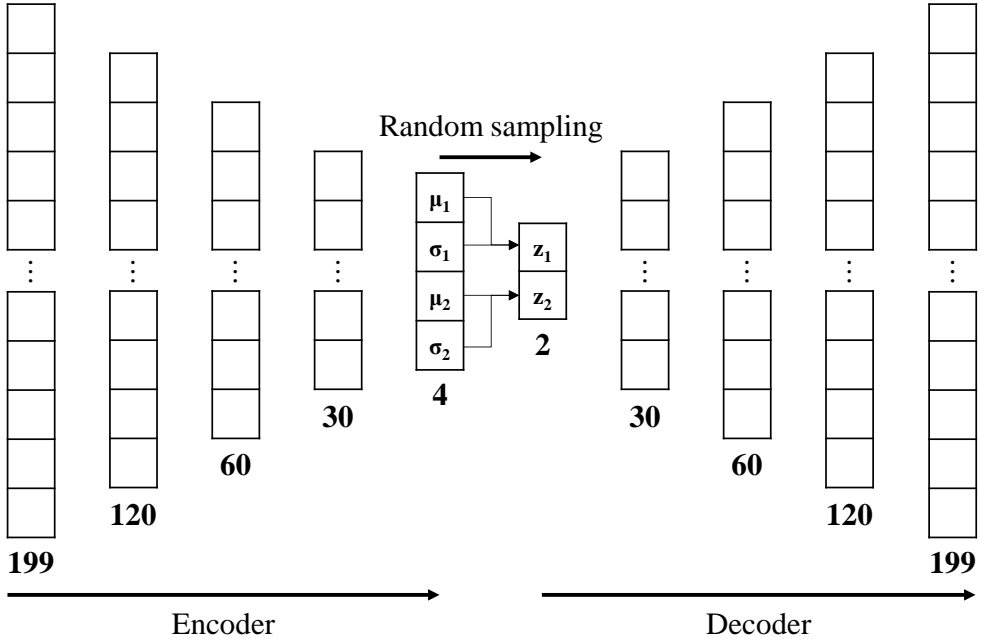


Fig. 6 Architecture of the VAE

4.3 Single-objective optimization results and discussion

Active learning of the single-objective optimization satisfies the error criterion (the error of the objective function at an optimum solution should be lower than 1%) after the 24 infilling iterations. The convergence history of optimization with active learning can be observed in Fig. 7. The objective function starts at approximately 65 and increases gradually, reaching a value of approximately 72 after 24 iterations. After that, a good optimal point was no longer found in the iterations. Subsequent analysis of the single-objective optimization results is based on the trained VAE and MLP at iteration 24 (total learning time for 24 iterations is $(508+627) + (186+226) * 24 = 11,023$ s).

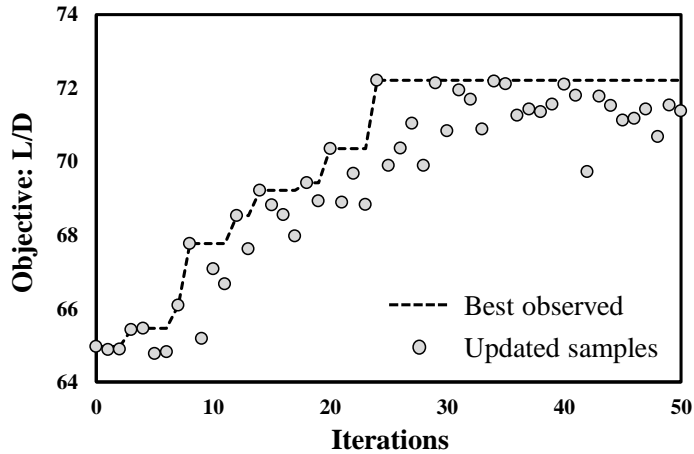


Fig. 7 Convergence history of single-objective optimization with active learning

The final optimal airfoil shape is shown in Fig. 8, and its QoI (objective function and constraints) values are summarized in Table 3. Its objective function (L/D) has a value of 72.22, which increased by 39% compared with the baseline. However, this value is just a prediction from the MLP model, and it is not certain whether the L/D from Xfoil will have this value. Therefore, the QoI from Xfoil were compared with the predicted values from the MLP model. It was confirmed that the four QoI values have an error (between predicted and calculated) of less than 1%, and all the imposed constraints were satisfied. Note that the airfoil area satisfies the constraint imposed with little margin (0.6%), whereas other constraints (drag and pitching moment) were satisfied with some margin. Additionally, numerical validation was performed to verify whether the optimal airfoil has the C_p distribution generated by the VAE model. Fig. 9 shows that the C_p generated by the VAE and that calculated using Xfoil are almost indistinguishable. These results validate the accuracy of the MLP model in the two-step approach for single-objective optimization.

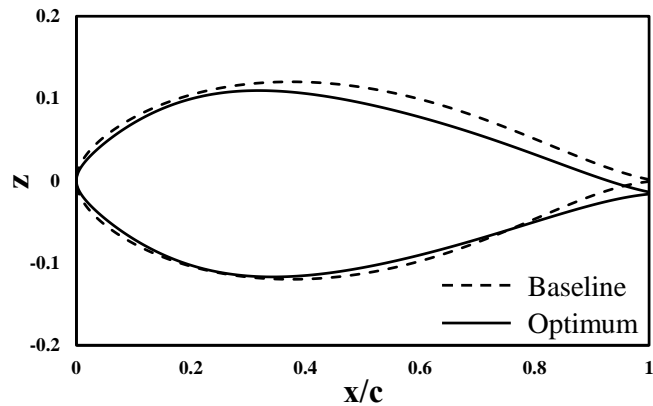


Fig. 8 Comparison of the baseline and optimum airfoil shape of single-objective optimization

Table 3 Summary of the QoI of the optimum solution

	L/D	C_d	C_m	Area [m ²]
Baseline	51.93	0.01436	-0.0040	0.1574
Optimum predicted	72.22	0.01301	-0.0173	0.1420
Optimum calculated	71.52	0.01305	-0.0172	0.1426
Error between predicted and calculated [%]	0.98	-0.28	0.72	-0.46
Comparison with baseline [%]	39.08	-9.40	332.50	-9.82

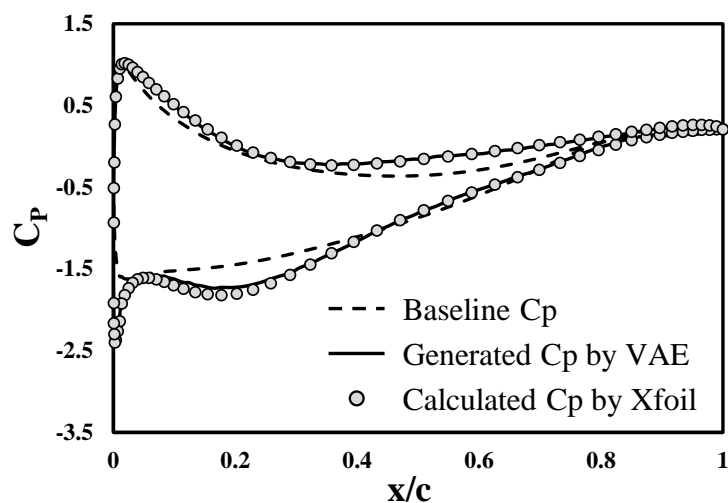


Fig. 9 Comparison of the generated and calculated pressure distribution of the optimum airfoil (baseline pressure distribution is also included)

Then, validation of the VAE model was performed. The VAE model reduces 199-dimensional C_p distribution data to a two-dimensional latent space and reconstructs it to 199-dimensional data. The trained decoder in this study was used as a data generator that receives a two-dimensional latent variable and creates 199-dimensional C_p distribution data. However, if the generated distribution cannot represent the overall training data or has completely different characteristics from them, the optimization results from this generator becomes inaccurate and inefficient. The randomly generated C_p distributions by the VAE decoder were analyzed to verify the validity of the generator. Fig. 10 shows 50 randomly selected C_p distributions (black lines) from the 500 initial training C_p data and 50 randomly generated C_p distributions (red lines) by the decoder. It was confirmed that the data generated using the decoder covers the range of the training data well. Moreover, although no other technique was applied to smoothen the C_p distribution in the VAE training, the decoder successfully generated smooth distributions indistinguishable from the training data. This supports the reason for adopting a VAE in this framework instead of a GAN; the VAE generates sufficiently realistic data (continuous C_p in this case) without adopting auxiliary layers or filters to

ensure the reality (continuity in this case) of the data.

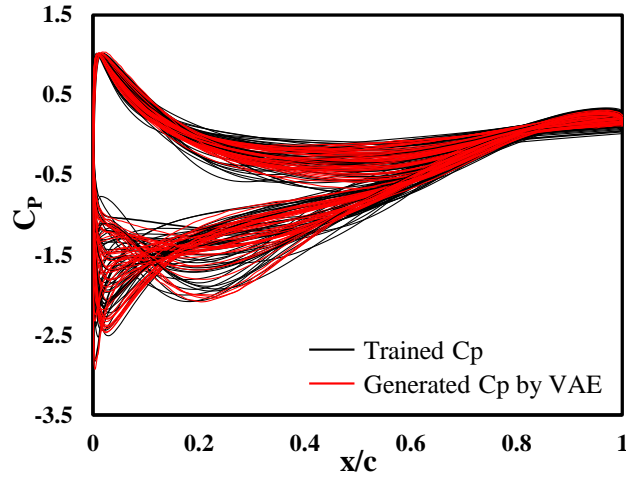


Fig. 10 Comparison of 50 randomly selected C_p training data (black lines) and 50 generated C_p distributions by the VAE (red lines)

The latent space of the decoder contains the crucial features necessary to reconstruct the original dimension of the training data (feature extraction). Therefore, in this study, the dominant features from the C_p distributions of the training data were visually investigated. Fig. 11 shows the C_p distributions generated according to a combination of two-dimensional latent space (latent variables 1 and 2 correspond to z_1 and z_2 in Fig. 6, respectively). Each variable was divided by 0.75 intervals in the range of -1.5–1.5, resulting in 25 C_p distributions. The horizontal and vertical axes of the C_p plots in Fig. 11 represent x/c and C_p , respectively and are scaled to the same range for comparison. It can be observed that the curvature near the suction peak (leading-edge of the lower curve) changes as latent variable 1 (z_1) varies; as z_1 decreases, the suction peak becomes sharper. On the other hand, when latent variable 2 (z_2) increases, the C_p value at the suction peak increases. Therefore, it was confirmed that the high-dimensional features

extracted from the training C_p data are the values and shapes of the suction peak. This can also be verified in Fig. 12, which shows 20 randomly selected C_p training data. Significant shape differences are observed in the selected data near the suction peak (near the leading-edge of the airfoil's upper surface) as indicated by the red dashed box, whereas most differences in the other regions are just slight shifts in the C_p values. It is concluded that the VAE model can operate successfully as a data generator in this framework, as shown in Figs. 10–12.

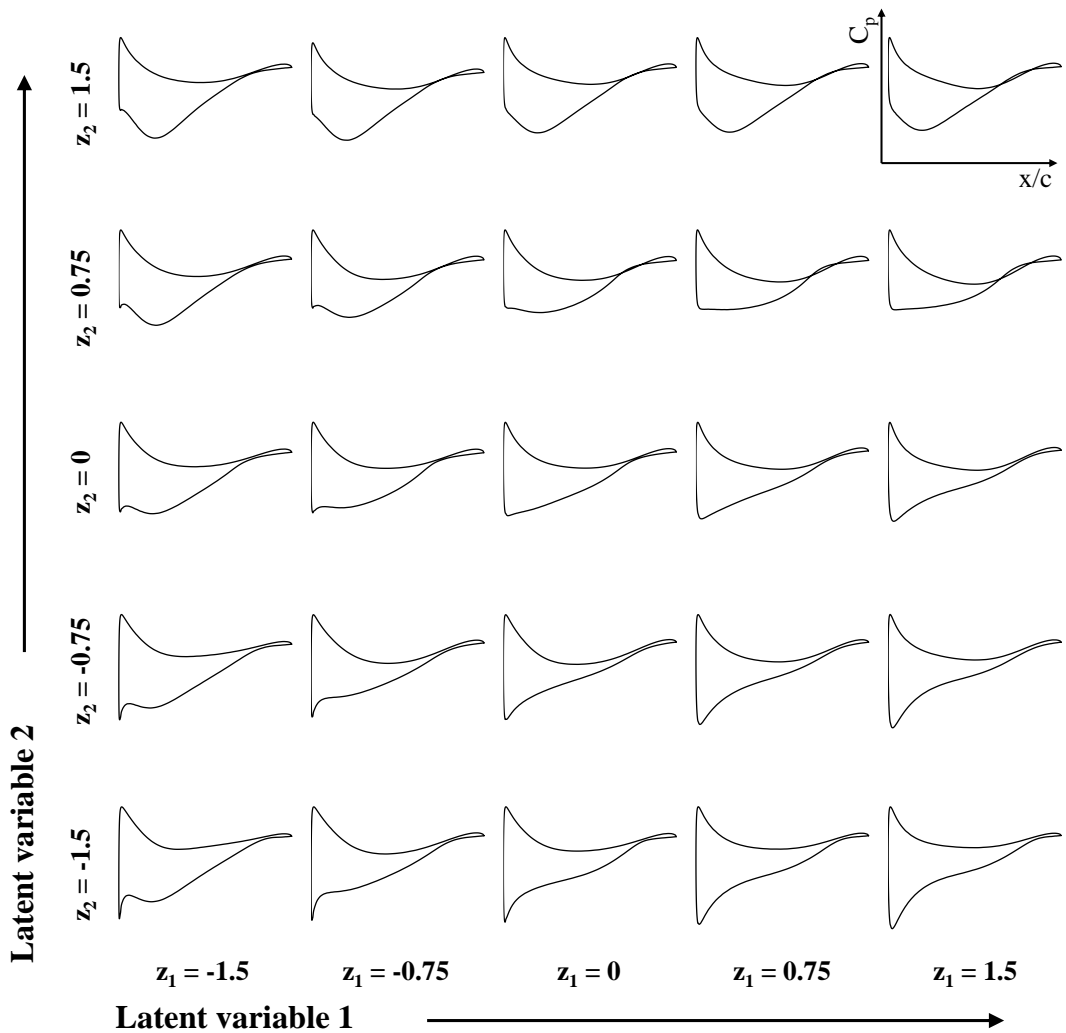


Fig. 11 Generated C_p by the VAE from various combinations of two latent variables; latent variable 1 (z_1) and latent variable 2 (z_2) are in the range of -1.5–1.5

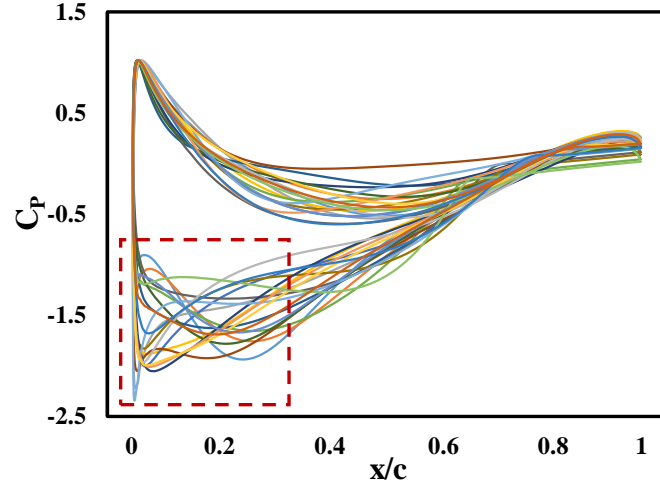


Fig. 12 Visualization of 20 randomly selected C_p training data. The red dashed box near the leading-edge of the lower curve indicates clear distinctions between them

4.4 Multi-objective optimization results and discussion

In section 4.3, it was confirmed that the proposed inverse design optimization framework yields outstanding results when single-objective optimization is performed. In this study, multi-objective optimization was also performed to ensure the universality of the framework in various optimizations, as presented in this section. In the previous single-objective problem, which uses L/D as an objective function and airfoil area as a constraint, the area of the optimum solution barely satisfies the constraint imposed. This indicates that an increase in the objective function L/D is suppressed by the area constraint. Therefore, in the multi-objective optimization, these two QoI were set as objective functions to consider their trade-off relationships (aerodynamic and structural performance). Refer to Table 2 for the problem definition of multi-objective optimization.

The active learning process of the multi-objective optimization converged after 59 iterations. Accordingly, 677 data consisting of initial 500 points and 177 infilled points were used (the total learning time for 59 iterations is $(508+627) + (186+226) * 59 = 25,443$ s). The resultant Pareto frontier of the two objective functions is shown in Fig. 13. We observed a discontinuity in the middle of the calculated Pareto solutions, and it is concluded that this is due to C_d constraint violation (the Pareto frontier from the optimization without the C_d constraint is smoothly connected). Among the Pareto solutions, six designs (A1–A3 and B1–B3) were selected for further analysis, and their airfoil shapes are shown in Fig. 14. Xfoil was performed on these six designs to estimate the error between the QoI from framework prediction and solver calculation, as in single-objective optimization. The corresponding results are summarized in Table 4. The airfoil shapes change smoothly from A1 to B3, and the errors between the QoI predicted using the framework and those obtained using Xfoil are within a reasonable range. In particular, A2 and B1 have quite large errors because there are few points added nearby in the active learning process (the percentage errors of C_m are also large, but this is because of their scale). The accuracy near these points can be increased by adding points close to them. It is up to the engineer where to infill points in the Pareto solutions. The accuracy of the trained MLP model was evaluated by verifying that the six selected designs actually have C_p distributions generated by the VAE. Fig. 15 shows that the MLP is accurate enough in that the C_p calculated using Xfoil and that generated using the VAE are almost indistinguishable, as in single-objective optimization.

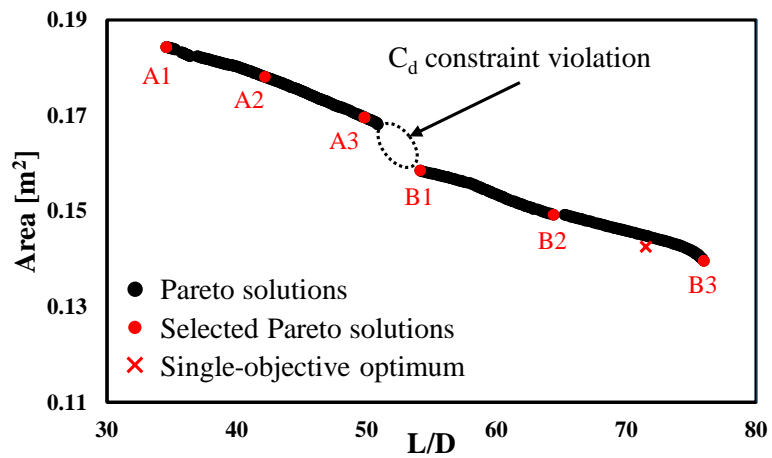


Fig. 13 Pareto solutions of multi-objective optimization. The discontinuity in the Pareto solutions is due to C_d constraint violation

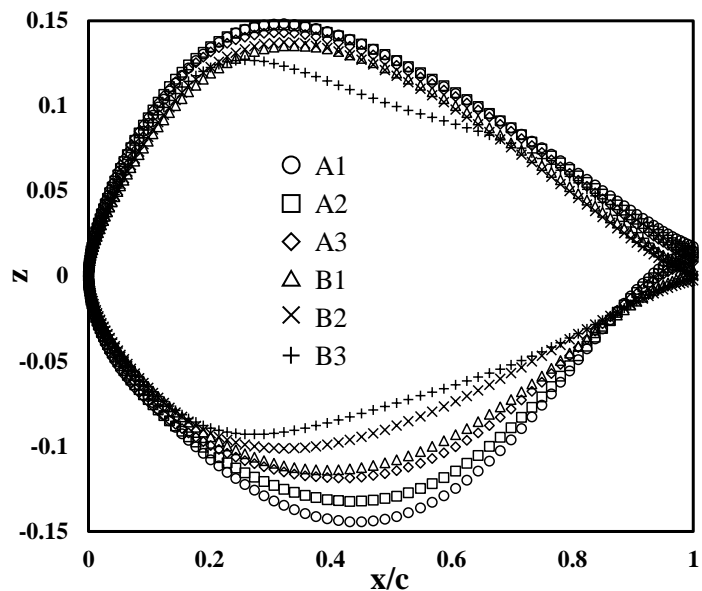


Fig. 14 Airfoil shape comparison of six selected Pareto solutions

Table 4 Summary of the QoI of six selected Pareto solutions

	L/D	Area [m ²]	C _d	C _m
Baseline	51.93	0.1574	0.01436	-0.0040
A1	Predicted	34.56	0.01436	0.0513
	Calculated	34.26	0.01445	0.0514
	Error [%]	-0.85	0.63	0.17
A2	Predicted	42.16	0.01434	0.0318
	Calculated	40.63	0.01461	0.0343
	Error [%]	-3.64	1.91	7.71
A3	Predicted	49.86	0.01423	0.0124
	Calculated	49.52	0.01428	0.0124
	Error [%]	-0.68	0.35	0.19
B1	Predicted	54.13	0.01436	-0.0027
	Calculated	55.22	0.01442	-0.0075
	Error [%]	2.01	0.43	179.92
B2	Predicted	64.42	0.01433	-0.0256
	Calculated	64.99	0.01445	-0.0333
	Error [%]	0.89	0.86	30.05
B3	Predicted	75.99	0.01307	-0.0387
	Calculated	76.32	0.01299	-0.0383
	Error [%]	0.43	-0.63	-1.12

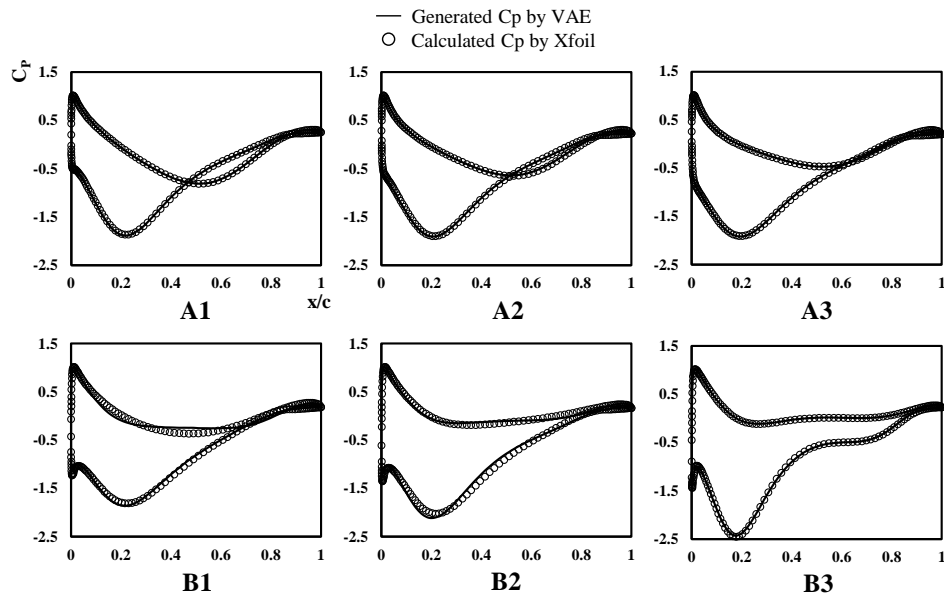


Fig. 15 Comparison of generated and calculated C_p distributions of six selected Pareto solutions

In this framework, the latent variable goes through the VAE decoder and MLP sequentially to predict the QoI values. Based on this two-step approach, an optimization technique (GA) was applied to obtain a latent variable that maximizes/minimizes the QoI. Therefore, for efficient optimization through this two-step deep learning approach, continuity between the two spaces (the latent space and QoI space) should be guaranteed to some extent. When these spaces are mapped very irregularly, the efficiency of the optimization technique can be significantly undermined. However, in real engineering problems, it is not always the case that variables are mapped smoothly. Abrupt changes, such as shock waves in transonic flow, are also frequently observed. In this context, this study investigated the mapping between the latent space and QoI through heatmaps, as shown in Fig. 16. It can be observed that the latent space is mapped continuously to both objectives, indicating how optimization in this framework could be performed successfully. On the other hand, sharp changes in both objectives are observed when z_2 has a value of approximately -0.55 (as indicated by the black square in Fig. 16). Therefore, a total of 12 points were extracted nearby, as shown at the top of Fig. 16, to investigate the changes that occur in the flowfield across this boundary. The nomenclatures of these 12 points are summarized in Table 5.

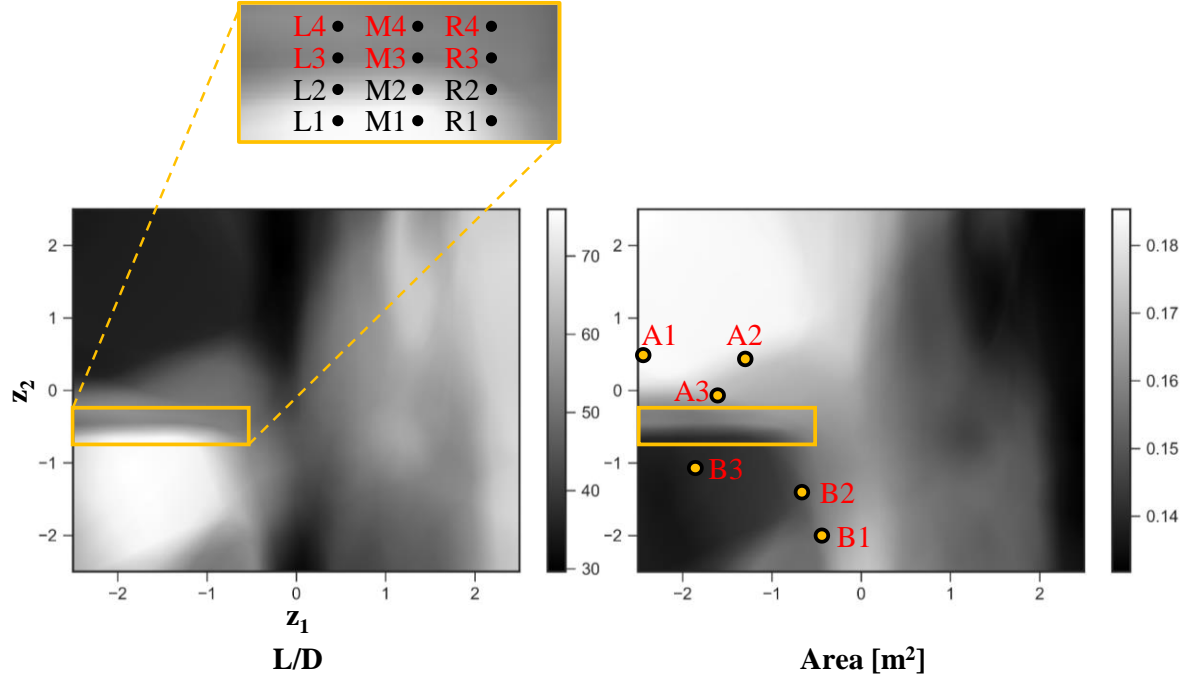


Fig. 16 Heatmaps of two objective functions within the latent space (left: L/D, right: area).

Twelve points were selected to investigate the rapid change at $z_2 \approx -0.55$ (top), and the latent space of six selected Pareto solutions is shown in the heatmap of the area (right)

Table 5 Nomenclatures of twelve points extracted to investigate the sharp changes in the

QoI heatmaps

		z_1		
		-2	-1.5	-1
		L4	M4	R4
z_2	-0.4	L4	M4	R4
	-0.5	L3	M3	R3
	-0.55	<i>Boundary of rapid change in the QoI heatmap</i>		
	-0.6	L2	M2	R2
	-0.7	L1	M1	R1

To investigate the reason for the sharp change in the QoI at $z_2 \approx -0.55$, the C_p distributions generated from the latent space nearby (12 selected points) using the VAE are shown in Fig. 17 (similar to Fig. 11, the horizontal and vertical axes of the plots represent x/c and C_p , respectively, and they are scaled to the same range). In this figure, the local leading-edge suction peaks on the lower curve are not observed in the C_p plots of $z_2 > -0.55$, whereas they are observed in the plots of $z_2 < -0.55$. Therefore, it can be inferred that $z_2 \approx -0.55$ is the boundary between the presence and absence of the leading-edge suction peak. In this regard, it is known that the sharper the leading-edge of the airfoil, the larger the suction peak behind the leading-edge (as the leading-edge radius decreases, the angle at which the flow should bend increases, thereby increasing the suction to attach the flow to the airfoil surface) [50]. Therefore, the trends in the leading-edge radius ($R_{L.E.}$) are depicted in Fig. 18 to verify whether the rapid change in C_p is accompanied by a change in $R_{L.E.}$. Indeed, in Fig. 18, as z_2 decreases (as the number corresponding to the second character of the name decreases), the leading-edge radius decreases, which is consistent with prior knowledge. Moreover, in all cases of L, M, and R, there are noticeable gaps between 2 and 3. Considering that nomenclatures 1, 2, 3, and 4 are equally spaced in the z_2 -direction, it can be concluded that a rapid change in the leading-edge radius at the boundary between 2 and 3 ($z_2 \approx -0.55$) leads to a sudden change in the trend of the leading-edge suction. Additionally, the six points selected from the Pareto solutions in Fig. 13 were scrutinized in a similar way. In Fig. 15, the leading-edge suction peak is not found in the C_p distributions of A1–A3, but is found in B1–B3. In fact, when the latent variables of these designs are visualized as shown in Fig. 16 (right), the two groups (A1–A3 and B1–B3) are separated by a boundary of $z_2 \approx -$

0.55. In summary, by analyzing the heatmaps, mapping between the latent space and QoI using the two-step approach is verified to be generally continuous. Additionally, this mapping is verified to accurately reflect the rapid change in the QoI, which occurs frequently in real-world engineering applications. This flexibility of the two-step deep learning approach enables the optimization to be performed efficiently owing to continuous and accurate mapping between the optimization inputs and outputs, highlighting the capability of the proposed inverse design optimization framework.

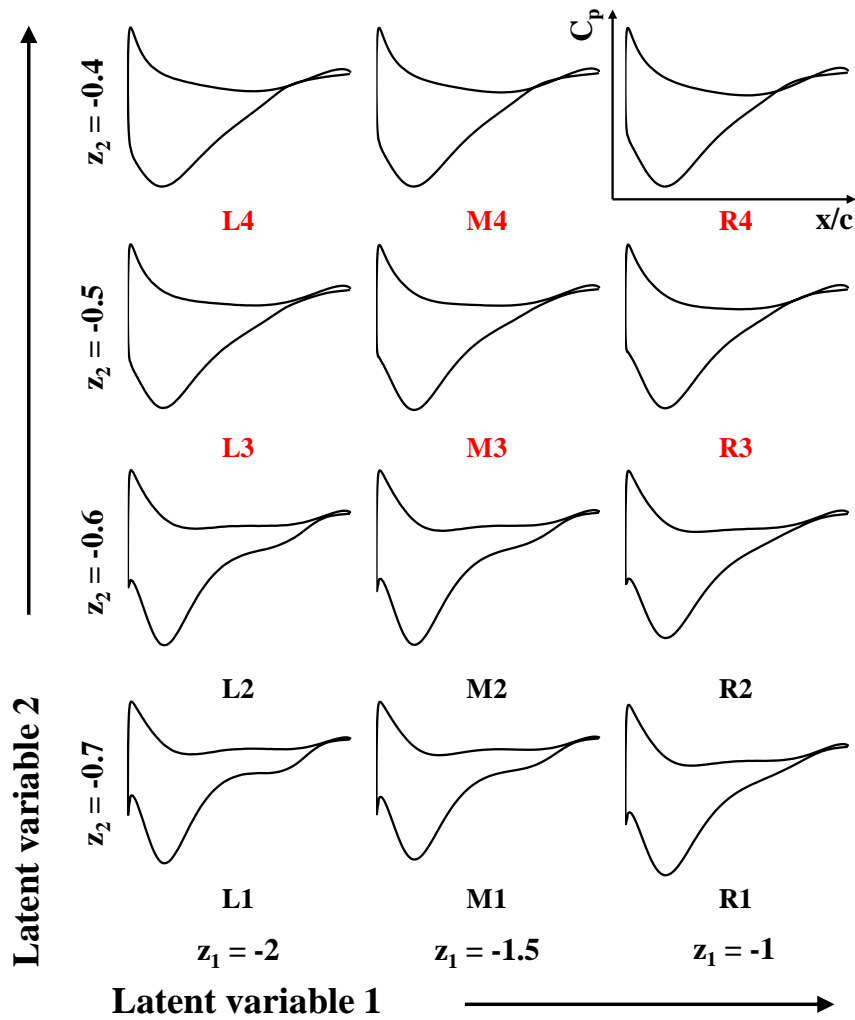


Fig. 17 C_p distributions of 12 selected points in Fig. 16

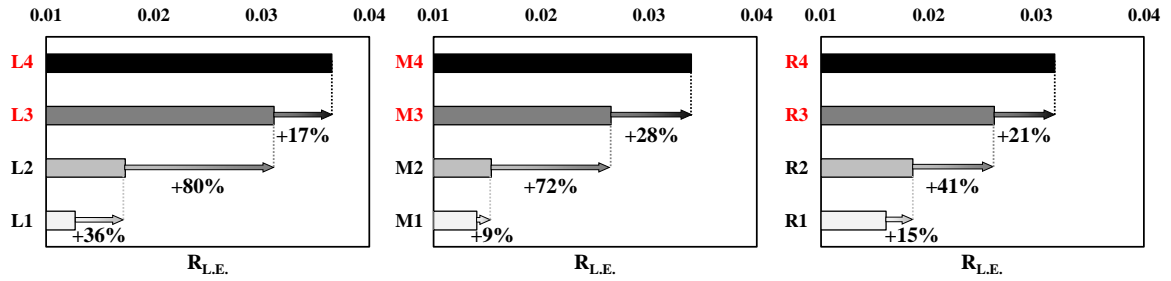


Fig. 18 Trends in the leading-edge radius ($R_{L.E.}$) of 12 selected points in Fig. 16

5. Conclusions

This study proposed a novel inverse design optimization framework with a two-step deep learning approach, which refers to consecutive coupling of two deep learning models, namely VAE and MLP. This framework overcomes the drawbacks of previous inverse design studies as follows: 1) with the MLP model, the iterative procedure of the conventional inverse design coupled with a flow solver is not required. Further, because the MLP predicts the QoI as well as the design shape, a theoretical/empirical assumption is not required and the geometric constraints in the inverse design optimization can be imposed directly; and 2) with the VAE model, realistic target performance distributions are generated, which alleviates the loss of the diverse representation capacity and removes the need for excessive constraints to ensure a realistic distribution.

In this study, the VAE and MLP were used sequentially to generate a realistic target distribution and to predict the QoI and shape parameters from the generated distribution, respectively. Then, the target distribution was optimized based on this two-step deep learning approach. To increase the accuracy of the two-step approach, we used active

learning to retrain the models with newly added designs. Also, transfer learning was applied to reduce the computational cost required for retraining. These techniques increase the accuracy of the framework using a reasonable computational resource.

The proposed framework was validated using two constrained optimization problems: single-objective and multi-objective airfoil optimization of the tip region of a megawatt-class wind turbine blade. In the single-objective optimization, the prediction accuracy of the trained MLP model and the validity of the trained VAE model for generating realistic data were verified. In the multi-objective results, continuous mapping between the inputs and outputs of the framework was verified, which enables successful optimization through the two-step approach. Furthermore, this mapping was confirmed to accurately reflect the rapid change in the QoI, which occurs frequently in real-world engineering applications. In summary, the results of the optimizations show that the proposed inverse design optimization framework via a two-step deep learning approach is accurate, efficient, and flexible enough to be applied to any other inverse design problem.

Considering that this novel framework can be coupled with any numerical solver with arbitrary design shape and QoI, it can be easily applied and extended to various engineering fields. Furthermore, the deep learning models in the two-step approach can be replaced by other suitable alternatives: the VAE by any data generator model and the MLP by any other regression model. For instance, the MLP, a widely used but quite simple model, was used in this study as the problem we investigated is not sufficiently complex to apply other advanced deep learning models. However, when the problem becomes complicated, other models such as convolutional neural networks or recurrent

neural networks can be used instead of the MLP model. This flexibility ensures that the framework can be employed with any model suitable for the engineering problem it applies to, contributing to the versatility of the framework.

Author contributions

Data curation [Sunwoong Yang]; Software [Sunwoong Yang]; Methodology [Sunwoong Yang]; Formal analysis [Sunwoong Yang]; Investigation [Sunwoong Yang]; Validation [Sunwoong Yang]; Visualization [Sunwoong Yang]; Writing – original draft [Sunwoong Yang]; Conceptualization [Sanga Lee]; Methodology [Sanga Lee]; Supervision [Sanga Lee]; Writing – review & editing [Sanga Lee]; Funding acquisition [Kwanjung Yee]; Project administration [Kwanjung Yee]; Resources [Kwanjung Yee]; Supervision [Kwanjung Yee]; Writing – review & editing [Kwanjung Yee]

References

- [1] A.H. Ibrahim, S.N. Tiwari, A variational method in design optimization and sensitivity analysis for aerodynamic applications, *Engineering with Computers* 20 (2004) 88–95.
<https://doi.org/10.1007/s00366-004-0273-7>.
- [2] V. Sekar, M. Zhang, C. Shu, B.C. Khoo, Inverse design of airfoil using a deep convolutional neural network, *AIAA J.* 57 (2019) 993–1003.
<https://doi.org/10.2514/1.J057894>.

[3] S.A. Renganathan, R. Maulik, J. Ahuja, Enhanced data efficiency using deep neural networks and Gaussian processes for aerodynamic design optimization, *Aerosp. Sci. Technol.* 111 (2021) 106522. <https://doi.org/10.1016/j.ast.2021.106522>.

[4] K. Daneshkhah, W. Ghaly, Aerodynamic inverse design for viscous flow in turbomachinery blading, *J. Propul. Power.* 23 (2007) 814–820. <https://doi.org/10.2514/1.27740>.

[5] Z. Li, X. Zheng, Review of design optimization methods for turbomachinery aerodynamics, *Prog. Aerosp. Sci.* 93 (2017) 1–23. <https://doi.org/10.1016/j.paerosci.2017.05.003>.

[6] K. Lane, D. Marshall, Inverse airfoil design utilizing CST parameterization. 48th AIAA Aerosp. Sci. Meeting Including the New Horiz. Forum and Aerospace Exposition, 2010. <https://doi.org/10.2514/6.2010-1228>.

[7] K. Hornik, M. Stinchcombe, H. White, Multilayer feedforward networks are universal approximators, *Neural Netw.* 2 (1989) 359–366. [https://doi.org/10.1016/0893-6080\(89\)90020-8](https://doi.org/10.1016/0893-6080(89)90020-8).

[8] A. Kharal, A. Saleem, Neural networks based airfoil generation for a given using Bezier–PARSEC parameterization, *Aerosp. Sci. Technol.* 23 (2012) 330–344. <https://doi.org/10.1016/j.ast.2011.08.010>.

[9] G. Sun, Y. Sun, S. Wang, Artificial neural network based inverse design: Airfoils and wings, *Aerosp. Sci. Technol.* 42 (2015) 415–428. <https://doi.org/10.1016/j.ast.2015.01.030>.

[10] X. Wang, S. Wang, J. Tao, G. Sun, J. Mao, A PCA-ANN-based inverse design model of stall lift robustness for high-lift device, *Aerosp. Sci. Technol.* 81 (2018) 272–283. <https://doi.org/10.1016/j.ast.2018.08.019>.

[11] S. Obayashi, S. Takanashi, Genetic optimization of target pressure distributions for inverse design methods, *AIAA J.* 34 (1996) 881–886. <https://doi.org/10.2514/3.13163>.

[12] H.J. Kim, O.H. Rho, Aerodynamic design of transonic wings using the target pressure optimization approach, *J. Aircr.* 35 (1998) 671–677. <https://doi.org/10.2514/2.2374>.

[13] Y. Zhu, Y. Ju, C. Zhang, Proper orthogonal decomposition assisted inverse design optimisation method for the compressor cascade airfoil, *Aerosp. Sci. Technol.* 105 (2020) 105955. <https://doi.org/10.1016/j.ast.2020.105955>.

[14] M.I. Jahirul, M.G. Rasul, R.J. Brown, W. Senadeera, M.A. Hosen, R. Haque, S.C. Saha, T.M.I. Mahlia, Investigation of correlation between chemical composition and properties of biodiesel using principal component analysis (PCA) and artificial neural network (ANN), *Renew. Energy.* 168 (2021) 632–646. <https://doi.org/10.1016/j.renene.2020.12.078>.

[15] X. Meng, G.E. Karniadakis, A composite neural network that learns from multi-fidelity data: Application to function approximation and inverse PDE problems, *J. Comp. Phys.* 401 (2020) 109020. <https://doi.org/10.1016/j.jcp.2019.109020>.

[16] A.L. Maas, A.Y. Hannun, A.Y. Ng, Rectifier nonlinearities improve neural network acoustic models, in: ICML Workshop on Deep Learning for Audio, Speech, and Language Processing (WDLASL 2013), 2013.

[17] D.P. Kingma, J.A. Ba, A Method for Stochastic Optimization. arXiv Preprint ArXiv:1412.6980 (2014).

[18] I. Goodfellow, Y. Bengio, A. Courville, Deep Learning, MIT Press, 2016.

[19] D.P. Kingma, M. Welling, An introduction to variational autoencoders, FNT in Machine Learning. 12 (2019) 307–392. <https://doi.org/10.1561/2200000056>.

[20] I.J. Goodfellow, J. Pouget-Abadie, M. Mirza, B. Xu, D. Warde-Farley, S. Ozair, A. Courville, Y. Bengio, Generative Adversarial Networks,” arXiv:1406.2661 (2014).

[21] D.P. Kingma, M. Welling, Auto-Encoding Variational Bayes. arXiv Preprint ArXiv:1312.6114 (2013).

[22] W. Chen, K. Chiu, M.D. Fuge, Airfoil design parameterization and optimization using Bézier generative adversarial networks, AIAA J. 58 (2020) 4723–4735. <https://doi.org/10.2514/1.J059317>.

[23] W. Chen, A. Ramamurthy, Deep generative model for efficient 3D airfoil parameterization and generation. AIAA Scitech 2021 Forum. Published, 2021. <https://doi.org/10.2514/6.2021-1690>.

[24] G. Achour, W.J. Sung, O.J. Pinon-Fischer, D.N. Mavris, Development of a conditional generative adversarial network for airfoil shape optimization. AIAA Scitech 2020 Forum. Published, 2020. <https://doi.org/10.2514/6.2020-2261>.

[25] M. Wiatrak, S.V. Albrecht, A. Nystrom, Stabilizing Generative Adversarial Networks: A Survey. arXiv Preprint ArXiv:1910.00927 (2020).

[26] M.A. Kramer, Nonlinear principal component analysis using autoassociative neural networks, *AIChE J.* 37 (1991) 233–243. <https://doi.org/10.1002/aic.690370209>.

[27] D.P. Kingma, T. Salimans, M. Welling, Variational Dropout and the Local Reparameterization Trick. *arXiv Preprint ArXiv:1506.02557* (2015).

[28] B. Settles, Active learning, *Synthesis Lectures on Artificial Intelligence and Machine Learning*. 6 (2012) 1–114. <https://doi.org/10.2200/S00429ED1V01Y201207AIM018>.

[29] X. Yang, X. Cheng, Z. Liu, T. Wang, A novel active learning method for profust reliability analysis based on the Kriging model, *Engineering with Computers* (2021). <https://doi.org/10.1007/s00366-021-01447-y>.

[30] S.J. Pan, Q. Yang, A survey on transfer learning, *IEEE Trans. Knowl. Data Eng.* 22 (2010) 1345–1359. <https://doi.org/10.1109/TKDE.2009.191>.

[31] Y. Li, W. Jiang, G. Zhang, L. Shu, Wind turbine fault diagnosis based on transfer learning and convolutional autoencoder with small-scale data, *Renew. Energy*. 171 (2021) 103–115. <https://doi.org/10.1016/j.renene.2021.01.143>.

[32] B. Moghadassian, A. Sharma, Designing wind turbine rotor blades to enhance energy capture in turbine arrays, *Renew. Energy*. 148 (2020) 651–664. <https://doi.org/10.1016/j.renene.2019.10.153>.

[33] L.E. Kollar, R. Mishra, Inverse design of wind turbine blade sections for operation under icing conditions, *Energy Convers. Manag.* 180 (2019) 844–858. <https://doi.org/10.1016/j.enconman.2018.11.015>.

[34] B. Moghadassian, A. Sharma, Inverse design of single- and multi-rotor horizontal axis wind turbine blades using computational fluid dynamics, *J. Sol. Energy Eng.* 140 (2018) 021003. <https://doi.org/10.1115/1.4038811>.

[35] M. Drela, XFOIL: An analysis and design system for low Reynolds number airfoils, in: T.J. Mueller (Ed.) *Low Reynolds Number Aerodynamics*. Lecture Notes in Engineering, vol 54, Springer, Berlin, Heidelberg, 1989. https://doi.org/10.1007/978-3-642-84010-4_1.

[36] A. Ceruti, Meta-heuristic multidisciplinary design optimization of wind turbine blades obtained from circular pipes, *Engineering with Computers* 35 (2019) 363–379. <https://doi.org/10.1007/s00366-018-0604-8>.

[37] W.J. Zhu, W.Z. Shen, J.N. Sørensen, Integrated airfoil and blade design method for large wind turbines, *Renew. Energy*. 70 (2014) 172–183. <https://doi.org/10.1016/j.renene.2014.02.057>.

[38] S. Mohammadi, M. Hassanalian, H. Arionfard, S. Bakhtiyarov, Optimal design of hydrokinetic turbine for low-speed water flow in Golden Gate Strait, *Renew. Energy*. 150 (2020) 147–155. <https://doi.org/10.1016/j.renene.2019.12.142>.

[39] R.J. McGhee, W.D. Beasley, Low-Speed Aerodynamic Characteristics of 17-Percent-Thick Airfoil Section Designed for General Aviation Applications, *NASA TN D-7428*, 1973.

[40] E. Tandis, E. Assareh, Inverse design of airfoils via an intelligent hybrid optimization technique, *Engineering with Computers* 33 (2017) 361–374. <https://doi.org/10.1007/s00366-016-0478-6>.

[41] S. Barone, Gear Geometric Design by B-Spline Curve Fitting and Sweep Surface Modelling, *Engineering with Computers* 17 (2001) 66–74.
<https://doi.org/10.1007/s003660170024>.

[42] Y. Li, K. Wei, W. Yang, Q. Wang, Improving wind turbine blade based on multi-objective particle swarm optimization, *Renew. Energy.* 161 (2020) 525–542.
<https://doi.org/10.1016/j.renene.2020.07.067>.

[43] P. Della Vecchia, E. Daniele, E. D’Amato, An airfoil shape optimization technique coupling PARSEC parameterization and evolutionary algorithm, *Aerosp. Sci. Technol.* 32 (2014) 103–110. <https://doi.org/10.1016/j.ast.2013.11.006>.

[44] F. Grasso, Usage of numerical optimization in wind turbine airfoil design, *J. Aircr.* 48 (2011) 248–255. <https://doi.org/10.2514/1.C031089>.

[45] H. Hamad, A. Al-Smadi, Space partitioning in engineering design via metamodel acceptance score distribution, *Engineering with Computers* 23 (2007) 175–185.
<https://doi.org/10.1007/s00366-007-0056-z>.

[46] L. Liu, H. Moayedi, A.S.A. Rashid, S.S.A. Rahman, H. Nguyen, Optimizing an ANN model with genetic algorithm (GA) predicting load-settlement behaviours of eco-friendly raft-pile foundation (ERP) system, *Engineering with Computers* 36 (2020) 421–433. <https://doi.org/10.1007/s00366-019-00767-4>.

[47] K. Deb, A. Pratap, S. Agarwal, T. Meyarivan, A fast and elitist multiobjective genetic algorithm: NSGA-II, *IEEE Trans. Evol. Computat.* 6 (2002) 182–197.
<https://doi.org/10.1109/4235.996017>.

[48] J. Blank, K. Deb, Pymoo: Multi-objective optimization in Python, IEEE Access. 8 (2020) 89497–89509. <https://doi.org/10.1109/ACCESS.2020.2990567>.

[49] A. Paszke, S. Gross, F. Massa, A. Lerer, J. Bradbury, G. Chanan, T. Killeen, Z. Lin, N. Gimelshein, L. Antiga, A. Desmaison, A. Köpf, E. Yang, Z. DeVito, M. Raison, A. Tejani, S. Chilamkurthy, B. Steiner, L. Fang, J. Bai, S. Chintala, PyTorch: An Imperative Style, High-Performance Deep Learning Library. arXiv Preprint ArXiv:1912.01703 (2019).

[50] N.G. Verhaagen, Effects of leading-edge radius on aerodynamic characteristics of 50° delta wings. J. Aircr. 49 (2012) 521–531. <https://doi.org/10.2514/1.C031550>.